

The role of Argon in CO₂ dissociation

Ana Silva, ana.f.sovelas.s@tecnico.ulisboa.pt
Instituto Superior Técnico, Lisboa, Portugal

October 2018

Abstract

The subject of creation of "solar fuels" from CO₂ is both trendy and relevant. The first step towards this goal is the conversion of CO₂ into CO. In this work we study the effects of Argon addition on CO₂ dissociation in low-pressure glow discharges through modelling and experiments. We measure the vibrational temperatures of CO₂, gas temperature and conversion factor ($\alpha = [\text{CO}]/[\text{CO}_2]$) with Fourier Transform Infrared spectroscopy and the density and temperature of Argon metastables with Tunable Diode Laser Absorption Spectroscopy. The experimental results show that lower pressure and flow as well as higher Argon content and current yield higher dissociation with measured conversions as high as $\approx 80\%$. Concerning energy efficiency, Argon addition is not beneficial at high currents (10 to 40 mA), but at the lowest currents studied the efficiencies seem unaffected by Argon. We also study the kinetic processes leading to these results using a simulation tool: LoKI. From the model's results validated by the experimental data, we conclude that the most important dissociation channels are electron impact dissociation and quenching of CO(a) by collision with CO₂. The addition of Argon improves conversion mostly via modification of the electron distribution function and does not affect significantly the vibrational populations of CO₂. Also, the results of a sensitivity analysis study, enabled us to draw some conclusions about the accuracy and precision of the model, and revealed the need for an accurate determination of the dissociation cross section via electron impact.

Keywords: CO₂/Ar plasma, Carbon dioxide conversion, plasma modelling, sensitivity analysis

Introduction

The ever-rising concentrations of CO₂ in the atmosphere are worrying scientists for a long time [1]. Recently, some interest has been put in the use of plasma technology as a solution to the CO₂ reduction problem [2] that can also help exploit the waste product molecule as a valuable carbon resource [3]. However, the elemental kinetic processes occurring in a CO₂ plasma are not yet completely understood and we have yet to pave the ways towards high conversion and energetically efficient processes. This work aims at giving a step towards this more complete understanding.

CO₂ dissociation and glow discharges

The splitting of CO₂ is a highly endothermic process. Thus, one important goal in CO₂ reduction technologies is that of designing a processing technique that splits CO₂ in an energetically efficient way and in large amounts, i.e. a process with high efficiency and conversion. The interactions between electrons, ions and neutral particles in a plasma can activate chemical reactions, even endothermic ones such as CO₂ dissociation, making plasma a natural environment where to ground a solution for this problem.

Many works [4, 5, 6] have tried to tackle the energy efficiency issue through the *V-V up-pumping mechanism* [7]: electron impact vibrational excitation (e-V) followed by collisions between 2 vibrationally excited molecules (V-V) that can lead to dissociation of CO₂. This is energetically favourable requiring only ≈ 5.5 eV/molecule, instead of the 7 eV required in direct electron impact dissociation. However, a detailed description of CO₂ vibrations is a difficult task because CO₂ has three modes of vibration: two degenerate bending modes, a symmetric stretch mode and an asymmetric stretch mode. Also

it is not yet clear how we can experimentally selectively excite vibration modes to the point of dissociation.

The activation of the plasma can be done using different set-ups, namely glow [8], dielectric barrier [4] and corona [9] discharges and plasma jets [10]. This work will focus on the characterization of the CO₂/Ar mixture in DC glow discharges. In Figure 1 we show the general structure of the plasma generated by this type of set-up.

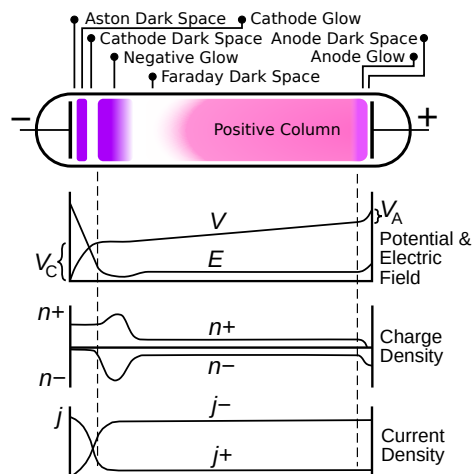


Figure 1: Structure of a glow discharge. + and - refer to positive ions and electrons, respectively. Adapted from [11].

In these discharges there exists a fixed cathode and a fixed anode in a gas chamber. At our working pressures (≈ 1 Torr) and with our relatively long discharge gap (≈ 20 cm), the chamber is mostly filled with the uniform glow of the positive column. This facilitates both diagnostics and modelling. The positive column region has a small and approximately constant electric field and electrons have energies of the order of 1 eV and retain most of the energy of the discharge. Thus, electron im-

compact processes play a very important role namely in the dissociation mechanisms [12]. In Figure 2 are some of the cross sections of electron impact with Ar and CO₂.

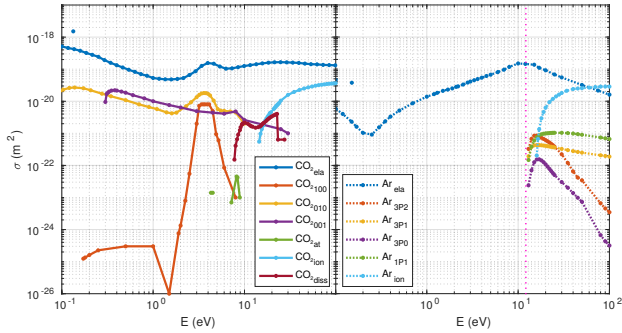


Figure 2: Cross sections for different electron collisional processes in an Ar/CO₂ mixture [13].

We are able to excite vibrations with electrons with energies of only about 1 eV - the typical energies in the positive column of a glow discharge-, while to achieve dissociation of CO₂ with a collision with one electron we need at least 7 eV. Still, the relaxation times at the working conditions of a glow discharge at low pressure are fast (about 0.1 μ s, 50 μ s and 1 ms respectively at 1 Torr). This makes the dissociation via vibrational excitation a difficult process to occur. Moreover, some more recent research [14] has claimed that the role of vibrations is not relevant unless inhomogeneous heating and turbulence effects are added to the equation.

Addition of Argon

The addition of Argon to the CO₂ plasma comes as a possible way of achieving higher conversions and efficiencies. Argon has been found to lower the breakdown voltage of the gas [15, 9, 16, 17]. which might be energetically beneficial. Due to Argon's low efficacy of recombination and the longer mean free paths of excited particles, gas temperature is expected to decrease and electron temperature to increase with Argon addition. These lower gas temperatures might increase vibrational populations and higher electron temperature might improve dissociation through direct electron impact. Moreover, the energy threshold for excitation and ionization of Argon is higher than the one for dissociation and vibrational excitation of CO₂ and thus Argon is not expected to be energy consuming [9].

Also, adding a different type of atom to the gas means

that there will be more chemical reactions happening, some of which may lead to CO₂ dissociation. However, some of these rates are not known and a systematic study of the addition of Argon to CO₂ plasma, focusing on modelling and verification, is still missing, although the first steps have already been taken [9, 18, 17].

Most of the experiments on CO₂ with addition of Argon were done using DBD reactors [15, 19, 20, 21], although some other configurations at atmospheric pressure [9, 22] or in thermal conditions [18] were also used. All works report higher or similar conversions and energy efficiencies upon addition of Argon. Adding Argon does not seem to produce trivial results and thus modelling becomes important to understand and optimize the dissociation process. All these facts lead us to believe that the Ar/CO₂ mixture would be one worth studying.

Optical Diagnostic Techniques

We can study the vibrations of CO₂ via the study of the interactions of photons with vibrational quanta. In this work we use FTIR spectroscopy, a technique that relies on the interference of radiation between two beams that pass through the plasma as schematically shown in Figure 3. We can then get the detected signal as a function of the change in path-length between the two beams - an interferogram. It is then possible to interchange between the path-length distance domain and a frequency domain performing a Fourier transformation.

The infrared transmittance spectrum is given by:

$$T = \frac{I}{I_0} = \frac{I_T - I_{plasma}}{I_0}, \quad (1)$$

where I is the intensity spectrum, containing contributions from the plasma emission I_{plasma} , and I_0 is the spectral profile of the IR source. This transmittance is then related with the properties of the absorbing medium via the Beer-Lambert law:

$$-\ln(T) = \int_0^\infty \mu(z) dz, \quad (2)$$

where z is the depth into the sample and μ is the absorption coefficient. The radiative transitions are not infinitely narrow, with several factors leading to a broadening. Since natural broadening is small when compared with Doppler and collisional broadening, it is usually neglected. This last two broadening phenomena

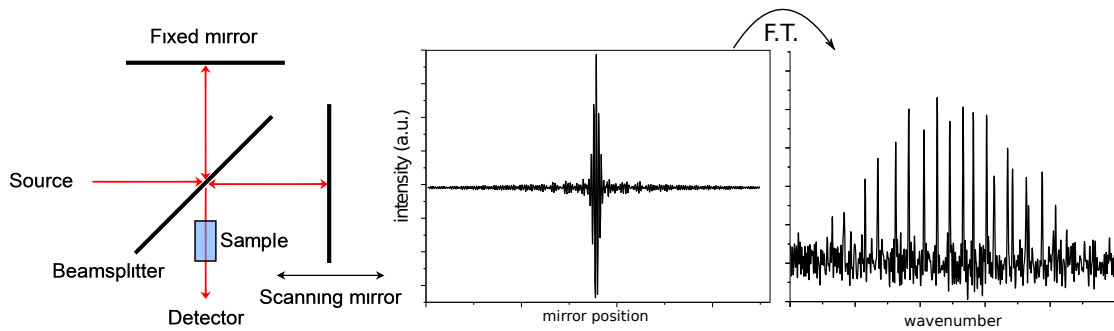


Figure 3: FTIR spectroscopy elements: the interferometer on the left, the resulting interferogram at the center and the spectrum of intensity as a function of the wave number.

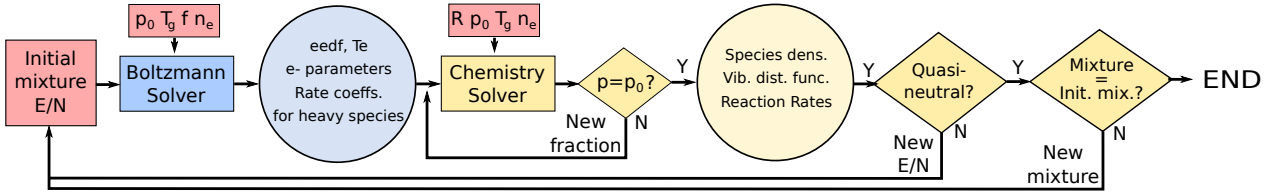


Figure 4: Work-flow of LoKI.

can be combined through convolution of its Gaussian and Lorentzian line-shapes, with a given Doppler and Lorentzian width, in what is usually called the Voigt function. In [8] it is explained how to successfully describe the shape of the spectral lines contained in CO₂ and CO bands and fit them to get rotational and vibrational temperatures as well as ground state densities.

In this work we also use tunable diode laser absorption spectroscopy (TDLAS). This technique relies on the use of a diode laser that is tuned by adjusting the injection current density into the gain medium to scan one absorption line corresponding to a given electronic state excitation of an atom. Once again, we use Beer-Lambert law (2) to relate the intensity after and before the laser has passed the plasma. In the specific case of this work, where only a specific transition from a lower state l to an upper state u is studied, the absorption coefficient per unit length is given by [23]:

$$\mu(\lambda, z) = \frac{g_u}{g_l} \cdot \lambda_0^2 \cdot \frac{A_{ul}}{8\pi} \cdot \left(n_l(z) - \frac{g_l}{g_u} \cdot n_u(z) \right) \cdot \phi_V(\lambda), \quad (3)$$

where λ_0 is the central wavelength of the absorption line, g is the degeneracy, A is the Einstein coefficient and ϕ_V is the Voigt lineshape. Here, we probe the excitation of the metastable states of Argon at the wavelengths of 772.42 and 772.38 nm. As the energy gap between the two levels is wide compared to the gas temperature we can neglect the population of the upper level in equation (3). We can then compute the densities of the metastable fitting an excitation transition line and computing its integral A :

$$N_l = A \cdot \frac{g_l}{g_u} \cdot \frac{8\pi}{\lambda_0^2 A_{ul} l}, \quad (4)$$

and get the temperature from the Doppler width of the line:

$$\Gamma_D = \frac{c}{\lambda_0} \sqrt{\frac{8kT \ln(2)}{mc^2}} \quad (5)$$

Plasma modelling and sensitivity analysis

A plasma model gives the solution of a system of self-consistently solved equations that are believed to describe the plasma under certain working conditions. This solution will ideally be able to reproduce measured characteristics of the plasma under the simulated conditions. Modelling provides powerful predictive abilities, explanation of the experimental observations in terms of the fundamental physics, that can help us in the designing and optimization of technological applications.

The modelling tool used in this thesis is LoKI. It couples the solution of the stationary electron Boltzmann equation under the usual two-term approximation with the system of rate balance equations for each specie in

the plasma. When solving for the EEDF, some assumptions are made [24], namely that we are in a steady state and that the plasma is homogeneous and only small anisotropies come from the electric field. Regarding the heavy species chemistry, in order to solve the rate balance equations we need to know which chemical reactions to include and each of the corresponding rate coefficients. In the case of electron impact processes, if the cross section of the collision is known, the rate coefficient can be obtained through the integration of the cross section over the distribution function. The work-flow of the code, illustrating how these Boltzmann and chemistry modules are coupled, is schematically shown in Figure 4. As output, the model can provide, among others, the densities of the heavy species, reaction rates, EEDF, power balance of electrons and self consistently calculated reduced electric field.

These low-temperature plasmas models usually contain hundreds of input parameters, each of them with an associated uncertainty that is often difficult to obtain. The propagation of error from all these hundreds of input variables to the output results can be of extreme relevance. In this work we also study the sensitivity of the model due to small changes in the input parameters to understand how each reaction influences the outputs. One influential work that delves in this topic is [25]. There Morris proposes an idea of how we can not only sample wisely and efficiently the input space parameters but also draw conclusions about what are the most important input variables. The second problem he solves with what he calls *elementary effects*. An elementary effect of a given input parameter x_i belonging to a vector of input parameters \mathbf{x} that produces an output y is:

$$d_i(\mathbf{x}) = \frac{[y(\mathbf{x} + \Delta) - y(\mathbf{x})]}{\Delta}, \quad (6)$$

where Δ is a vector with all entries 1 except for the i th which is Δ . This variable describes how changes in the input variables x_i affect the outputs. As for sampling, he proposes an individually randomized one-factor-at-a-time sampling method. The parameter space is swept in the following manner:

1. A point in the input parameter space is randomly chosen;
2. The output corresponding to that initial set of input values is computed;
3. One and only one of the variables is changed and the output is computed again and compared with the previous output to obtain one elementary effect;
4. The last step is repeated until all of the k inputs were changed once;
5. All the previous steps are repeated r times.

Experimental results

For both FTIR and TDLAS measurements the reactor used consists of a Pyrex cylinder with one electrode placed at each end. In Figure 5 is a representation of the set-up.

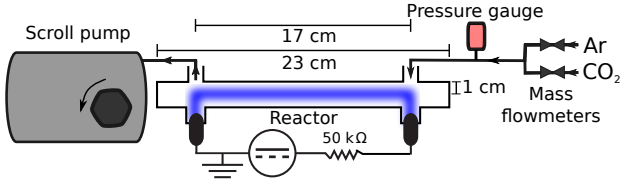


Figure 5: Representation of the reactor used to obtain the experimental results presented in this work.

The high voltage electrode is connected to a power supply (Fug HCP 300-6500) and the current is limited by a ballast resistor of 50 kΩ in series with the reactor. Two bottles, one of pure Argon (Air Liquide Alphagaz 2) and one of pure CO₂ (Air Liquide Alphagaz 2), are connected each to one mass flow-meter (Bronkhorst, F-201CV) and the mixture enters the reactor near the high voltage electrode. The pressure is measured with a pressure gauge (Pfeiffer, CMR 263) and controlled with a manual valve and a scroll pump (Edwards, nXDS).

FTIR spectroscopy - Conversion and temperatures

In Figure 6 is an example of a spectrum corresponding to CO and CO₂ bands as well the fit obtained using the algorithm explained in [8]. For all the data shown in this work it is assured that the amplitude of the residual is below 5% of the amplitude of the spectra.

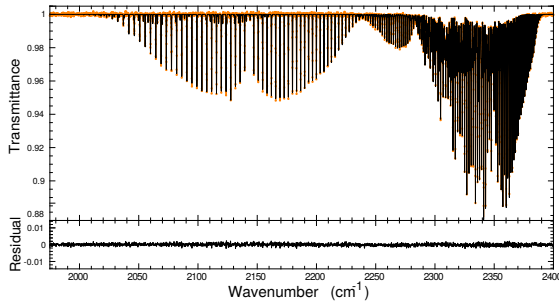


Figure 6: Example spectrum. In yellow is the experimental data and in black the fit. On the left - CO bands corresponding mostly to rotational transitions. On the right - CO₂ bands corresponding to absorption of a photon by the asymmetric stretch mode.

Temperatures are taken *in-situ*, while the conversion factors are measured downstream of the reactor. The conversion (α) and energy efficiency (η) are estimated in the following manner:

$$\alpha = \frac{[CO]_{out}}{[CO_2]_{in}} \approx \frac{[CO]_{out}}{[CO_2]_{out} + [CO]_{out}} \quad (7)$$

$$\eta = \frac{\alpha E_d}{SEI} = \frac{\alpha E_d}{P_{reactor} Q_N} \approx 3.02 \frac{\alpha f_{CO_2} f [sccm]}{P_{reactor} [W]}, \quad (8)$$

where *in* and *out* stand for input and output concentrations, *SEI* is the specific energy input, E_d the energy needed for dissociation, $P_{reactor}$ is the power spent in the whole reactor, and f the gas flow. $P_{reactor}$ is the product of the current passing through the reactor by

the potential difference between the electrodes. In Figures 7 and 8 we show some of the fitting results for the conversion factor and energy efficiency.

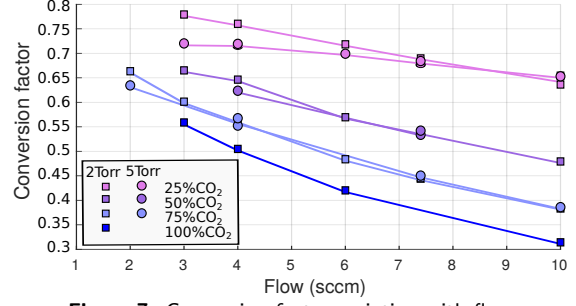


Figure 7: Conversion factor variation with flow

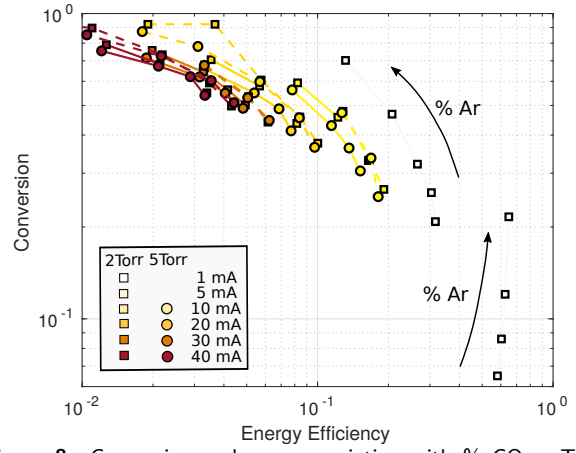


Figure 8: Conversion and energy variation with % CO₂. The dashed and solid lines correspond to measurements at 4 and 7.4 sccm respectively. δ_{CO_2} is the fraction of CO₂ injected.

Both flow and Argon content are causing a significant variation of the conversion factor, while the pressure does not seem to affect this quantity. From 0 to 75% Argon content the conversion rises about 0.25 regardless of the working conditions. The energy efficiency goes down with argon addition, except for the lowest current. This is because, although conversion is higher, the actual number of CO molecules produced, goes down with the amount of Argon added.

We also get the rotational (see Figure 9) and vibrational temperatures from the fitting.

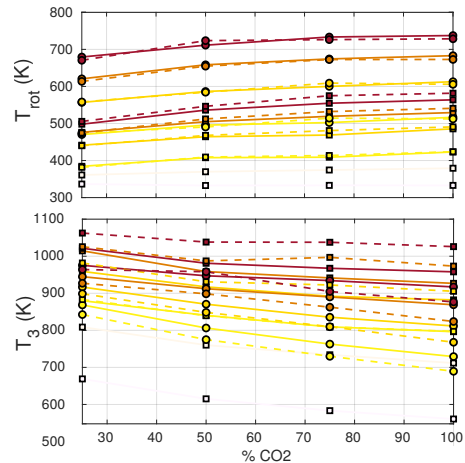


Figure 9: Rotational/translational temperature.

The measurements show that both the rotational temperature and $T_{1,2}$ go down with Argon addition about 40 K for 10 mA or higher. T_3 increases as more Argon is added, which might be an indicator of some accumulation of energy in this vibrational mode. As for the flow, it does not seem to change neither the gas temperature nor $T_{1,2}$.

We also estimate the electric field inside the reactor computing the potential difference between two metal rods 8 cm apart and radially pointing inside the positive column of the plasma. Taking the temperature of the gas to be equal to the rotational temperatures shown in Figure 9, we compute the reduced electric-field. The results are shown in Figure 10.

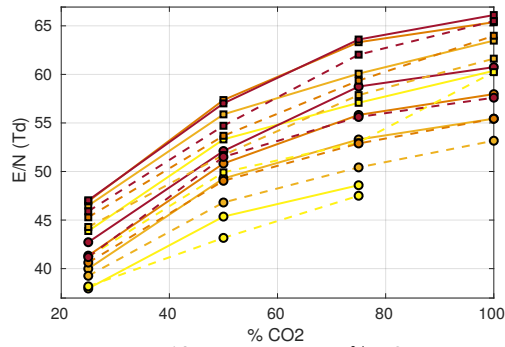


Figure 10: Variation with % CO₂

The reduced electric field drops ≈ 15 -20 Td for all conditions as we change the gas composition from 100 to 25 % CO₂. The flow affects E/N only slightly - about 5 to 10 Td difference between the lowest and highest flow measured for a given pressure, % Ar and current.

TDLAS - Study of Ar^m densities and temperatures

Now we turn our attention to the characterization of the Argon metastable states using TDLAS. The set-up used for the measurements presented in this section is depicted in Figure 11. The light-source is a tunable diode laser (Toptica Photonics DL 100) with a wavelength around 772 nm. The laser-light is collected at the end of the reactor by a fast photo-diode (rise time of ≈ 1 ns) which is connected to an oscilloscope (Lecroy Waverunner 500MHz). The injection current of the diode laser is scanned with a triangular signal sent by a function generator that also triggers the oscilloscope. We use a Fabri-Perrot interferometer calibrated with a wavelengthmeter to translate the time axis in the oscilloscope to wavelength. To avoid power broadening, the power of the laser beam was attenuated and the line widths and intensities were measured for several different intensities

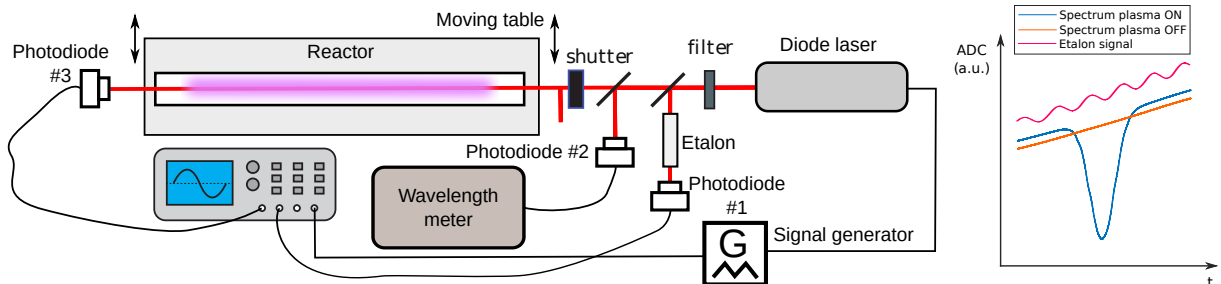


Figure 11: Set-up for Ar^m density and temperature measurements and acquisition example.

of the beam. As there was no noticeable increase of these quantities with the power of the laser it was assumed that power broadening could be neglected. Also, the reactor is attached to a table that is able to move perpendicularly to the reactor's axis, so we can sweep over the radial coordinate. In Figure 12 we show an example of a Voigt function fit to the transmittance. The fitting tool used is open software available online [26].

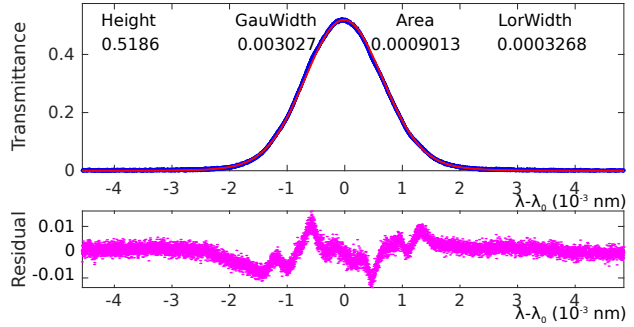


Figure 12: Example of a typical fit to a Voigt profile.

The measurements shown in this section correspond to fitting results whose fitting error was below 2%. In Figure 13 we show some of these results.

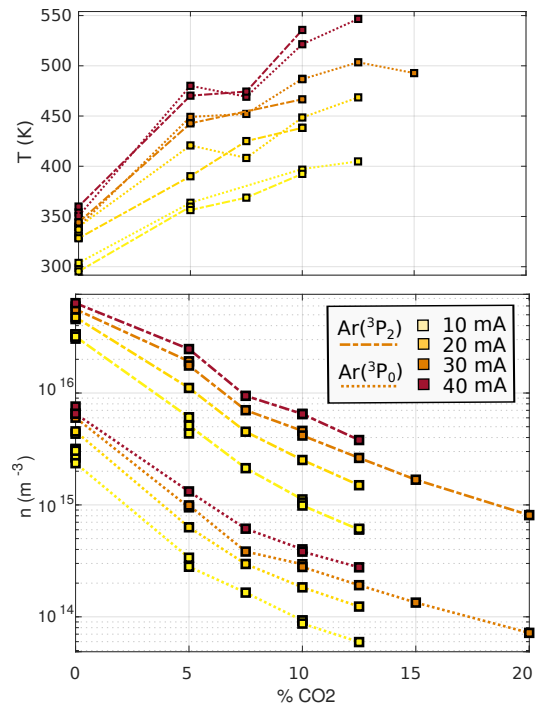


Figure 13: Metastable temperatures and densities.

For very low content of CO₂ the temperature curves

are steep and the gas cools down almost to room temperature. As for the densities, the added CO₂ strongly quenches the metastables. Although we cannot measure with TDLAS and FTIR spectroscopy the temperatures for the same Ar/CO₂ fraction, we can compare the results obtained with both diagnostics. Both temperature data are consistent, although the metastable temperatures are slightly higher than expected.

The argon metastable states are highly affected by pressure, with the densities dropping about one order of magnitude from 1 to 5 Torr. The flow seems to cause no significant change in the densities of these atoms.

Modelling

Kinetic scheme for Ar/CO₂ mixture

The kinetic scheme used in this work is comprised of the compilation of several models. In Tables 1-2 we present the final kinetic scheme concerning Argon, CO₂ and the mixture. These reactions, together with the kinetics for Oxygen in [27] and the electron kinetics of CO in [28], constitute the whole kinetic scheme used in this work. The label 'CS' is used in the processes whose rate coefficients are obtained via the integration of a cross section over the EEDF. The label 'B' is used whenever a given cross section was used to compute the EEDF in the Boltzmann-module of LoKI and the label 'C' marks the processes used in the chemistry-module to compute the heavy species' densities.

Electron density calculation and flow description

As already mentioned in the background section, to run LoKI we need as input parameters: pressure, temperature, initial fraction of CO₂/Ar and electron density. The first three are known from experiment. The input electron density is computed in an iterative manner. First, we run LoKI with a guess for electron density - n_e - and obtain the corresponding drift velocity from the model - v_d . Then, a new guess for the density is made - $n_e = \frac{I_{exp}}{ev_d \pi R^2}$ - and we run the model again. We do this until the value for the current obtained with v_d and n_e matches the current measured in the experiment within 1% error.

Since conversions are highly affected by the renovation of the gas in the reactor we need to include a flow description. We decided to do this with an extra term in the rate balance equations. As we impose the flow in the reactor and taking advantage of the fact that we have $n_{CO} \approx 2 \times n_{O_2}$, this process is included in the model as an effective reaction $CO + \frac{1}{2}O_2 \rightarrow CO_2$ with a rate coefficient constructed such that the variation in the density of CO₂ is due to gas renewal.

Comparison of model and experiment

In this section we use the model aforescribed and compare the outputs with the experimental data. We compare the reduced electric field, conversion and Argon metastable densities. In deciding which dissociation cross section to use, we tried:

1. The cross section proposed by Polak [40].
2. The same cross section as in 1. multiplied by 2.

COLLISION	USE	REF.
$e + Ar(1S_0) \rightarrow e + Ar(1S_0)$	B	
Electronic collisional processes - Excitation		
$e + Ar(1S_0) \leftrightarrow e + Ar(3P_2)$	B+C	[29]
$e + Ar(1S_0) \leftrightarrow e + Ar(3P_1)$	B+C	[29]
$e + Ar(1S_0) \leftrightarrow e + Ar(3P_0)$	B+C	[29]
$e + Ar(1S_0) \leftrightarrow e + Ar(1P_1)$	B+C	[29]
$e + Ar(1S_0) \leftrightarrow e + Ar^*$	B	[29]
$e + Ar(3P_2) \leftrightarrow e + Ar(3P_1)$	B+C	[29]
$e + Ar(3P_2) \leftrightarrow e + Ar(3P_0)$	B+C	[29]
$e + Ar(3P_2) \leftrightarrow e + Ar(1P_1)$	B+C	[29]
$e + Ar(3P_1) \leftrightarrow e + Ar(3P_0)$	B+C	[29]
$e + Ar(3P_1) \leftrightarrow e + Ar(1P_1)$	B+C	[29]
$e + Ar(3P_0) \leftrightarrow e + Ar(1P_1)$	B+C	[29]
$e + Ar(1S_0) \leftrightarrow e + Ar(4p)$	C	[29]
$e + Ar(3P_2) \leftrightarrow e + Ar(4p)$	C	[29]
$e + Ar(3P_1) \leftrightarrow e + Ar(4p)$	C	[29]
$e + Ar(3P_0) \leftrightarrow e + Ar(4p)$	C	[29]
$e + Ar(1P_1) \leftrightarrow e + Ar(4p)$	C	[29]
Electronic collisional processes - Ionization		
$e + Ar(1S_0) \rightarrow e + e + Ar^+$	B+C	[29]
$e + Ar(3P_2) \rightarrow e + e + Ar^+$	B+C	[29]
$e + Ar(3P_1) \rightarrow e + e + Ar^+$	B+C	[29]
$e + Ar(3P_0) \rightarrow e + e + Ar^+$	B+C	[29]
$e + Ar(1P_1) \rightarrow e + e + Ar^+$	B+C	[29]
$e + Ar(4p) \rightarrow e + e + Ar^+$	C	[29]
Molecular conversion		
$Ar^+ + 2Ar(1S_0) \rightarrow Ar_2^+ + Ar(1S_0)$	C	[30]
Dissociative recombination		
$e + Ar_2^+ \rightarrow Ar(3P_2) + Ar(1S_0)$	C	[30]
$e + Ar_2^+ \rightarrow Ar(3P_1) + Ar(1S_0)$	C	[30]
$e + Ar_2^+ \rightarrow Ar(3P_0) + Ar(1S_0)$	C	[30]
$e + Ar_2^+ \rightarrow Ar(1P_1) + Ar(1S_0)$	C	[30]
$e + Ar_2^+ \rightarrow Ar(4p) + Ar(1S_0)$	C	[31]
$e + Ar_2^+ \rightarrow 2Ar(1S_0)$	C	[30]
Penning ionization		
$Ar(4s_i) + Ar(4s_j) \rightarrow Ar(1S_0) + Ar^+ + e$	C	[31]
$2Ar(4p) \rightarrow e + Ar^+ + Ar(1S_0)$	C	[31]
$Ar(4s_i) + Ar(4p) \rightarrow e + Ar^+ + Ar(1S_0)$	C	[31]
$Ar(4s_i) + Ar(4s_j) \rightarrow e + Ar_2^+$	C	[30]
Atomic Impact Excitation		
$Ar(4p) + Ar(1S_0) \rightarrow Ar(4s_i) + Ar(1S_0)$	C	[31]
Atomic Conversion		
$Ar_2^+ + Ar(1S_0) \rightarrow Ar^+ + 2Ar(1S_0)$	C	[31]
3-body recombination		
$e + e + Ar^+ \rightarrow e + Ar(4s_i)$	C	[30]
$e + e + Ar^+ \rightarrow e + Ar(4p)$	C	[30]
Radiative processes		
$Ar(3P_1) \rightarrow Ar(1S_0) + h\nu$	C	[32] [33]
$Ar(1P_1) \rightarrow Ar(1S_0) + h\nu$	C	[32] [33]
$Ar(4p) \rightarrow Ar(3P_2) + h\nu$	C	[30]
$Ar(4p) \rightarrow Ar(3P_1) + h\nu$	C	[30]
$Ar(4p) \rightarrow Ar(3P_0) + h\nu$	C	[30]
$Ar(4p) \rightarrow Ar(1P_1) + h\nu$	C	[30]
E-impact dissociation		
$e + Ar_2^+ \rightarrow e + Ar(1S_0) + Ar^+$	C	[31]
Recombination		
$e + Ar^+ + Ar(1S_0) \rightarrow 2Ar(1S_0)$	C	[9]
Diffusion		
Diffusion of $Ar(3P_2)$ and $Ar(3P_0)$	C	[34]
Ambipolar diffusion of Ar^+ and Ar_2^+	C	[34]

Table 1: Argon kinetic scheme. Ar* denotes an electronically excited state above Ar(4s).

3. Using the cross section for excitation of CO₂ into the first electronically excited state.

The cross section of Polak highly underestimates conversion. Assuming the same shape for the cross section but doubling its value produced better results. The best agreement, however, was obtained assuming that the first electronic excitation of CO₂ is the dissociative

COLLISION	USE	REF.
Electronic collisional processes - Excitation		
$e + \text{CO}_2 \rightarrow e + \text{CO}_2$	B	[35]
e-impact excitation		
$e + \text{CO}_2 \rightarrow e + \text{CO}_2(X, v=1-16)$	B	[35]
$e + \text{CO}_2 \rightarrow e + \text{CO}_2(e1)$	B	[35]
$e + \text{CO}_2 \rightarrow e + \text{CO}_2(e2)$	B	[35]
Ionization		
$e + \text{CO}_2 \rightarrow e + e + \text{CO}_2^+$	B+C	[35]
$e + \text{CO}_2 \rightarrow e + e + \text{CO} + \text{O}^+$	B+C	[36]
$e + \text{CO}_2 \rightarrow e + e + \text{CO}^+ + \text{O}$	B+C	[36]
$e + \text{CO}_2 \rightarrow e + e + \text{O}_2^+ + \text{C}$	C	[6]
Attachment		
$e + \text{CO}_2 \rightarrow \text{CO} + \text{O}^-$	B	[35]
$e + \text{CO}_4^+ \rightarrow \text{CO}_2 + \text{O}_2$	C	[6]
Dissociation		
$e + \text{CO}_2 \rightarrow e + \text{CO} + \text{O}$	C	(see text)
Neutral-neutral reactions		
$\text{CO}(a) + \text{O}_2 \rightarrow \text{CO}_2 + \text{O}$	C	[37]
$\text{CO}(a) + \text{CO} \rightarrow \text{CO}_2 + \text{C}$	C	[37]
$\text{CO}(a) + \text{O}_2 \rightarrow \text{CO} + \text{O}_2$	C	[37]
$\text{CO}(a) + \text{O}_2 \rightarrow \text{CO} + 2\text{O}$	C	[37]
$\text{CO}(a) + \text{CO} \rightarrow 2\text{CO}$	C	[37]
$\text{CO}(a) + \text{CO}_2 \rightarrow \text{CO} + \text{CO}_2$	C	[37]
$\text{CO}(a) + \text{CO}_2 \rightarrow 2\text{CO} + \text{O}$	C	[37]
$\text{O} + \text{O}_2 + \text{CO}_2 \rightarrow \text{O}_3 + \text{CO}_2$	C	[6]
$\text{O} + \text{CO} + \text{CO}_2 \rightarrow 2\text{CO}_2$	C	[6]
$\text{O} + 2\text{CO} \rightarrow \text{CO}_2 + \text{CO}$	C	[6]
$\text{C} + \text{CO} + \text{CO}_2 \rightarrow \text{C}_2\text{O} + \text{CO}_2$	C	[6]
$\text{O} + \text{C}_2\text{O} \rightarrow 2\text{CO}$	C	[6]
$\text{O}_2 + \text{C} \rightarrow \text{CO} + \text{O}$	C	[6]
$\text{O}_2 + \text{C}_2\text{O} \rightarrow \text{CO}_2 + \text{CO}$	C	[6]
Ion-neutral & ion-ion reactions		
$\text{CO}^+ + \text{O}_2 \rightarrow \text{O}_2^+ + \text{CO}$	C	[37]
$\text{O}^+ + \text{CO}_2 \rightarrow \text{O}_2^+ + \text{CO}$	C	[6]
$\text{O}^+ + \text{CO}_2 \rightarrow \text{CO}_2^+ + \text{O}$	C	[6]
$\text{CO}_2^+ + \text{O}_2 \rightarrow \text{O}_2^+ + \text{CO}_2$	C	[6]
$\text{CO}^+ + \text{CO}_2 \rightarrow \text{CO}_2^+ + \text{CO}$	C	[6]
$\text{O}_2^+ + 2\text{CO}_2 \rightarrow \text{CO}_4^+ + \text{CO}_2$	C	[6]
$\text{O}_2^+ + \text{CO}_2 + \text{CO} \rightarrow \text{CO}_4^+ + \text{CO}$	C	[6]
$\text{O}_2^+ + \text{CO}_2 + \text{O}_2 \rightarrow \text{CO}_4^+ + \text{O}_2$	C	[6]
Recombination of CO and O into CO₂ at the wall		
$\text{CO} + \text{O} + \text{wall} \rightarrow \text{CO}_2$	C	[37]
Diffusion		
Ambipolar diffusion of $\text{CO}^+, \text{CO}_2^+$	C	[38]
Quenching of metastables		
$\text{Ar}(^3P_2) + \text{M} \rightarrow \text{Ar} + \text{M}$	C	[39]
$\text{Ar}(^3P_0) + \text{M} \rightarrow \text{Ar} + \text{M}$	C	[39]
Dissociation by collision with metastable		
$\text{Ar}(^3P_2) + \text{CO}_2 \rightarrow \text{Ar} + \text{CO} + \text{O}$	C	[17]
$\text{Ar}(^3P_0) + \text{CO}_2 \rightarrow \text{Ar} + \text{CO} + \text{O}$	C	[17]

Table 2: CO₂/Ar kinetic scheme. CO₂(X,v=1-16) refers to the first 16 vibrationally excited states of CO₂. M=CO₂,O₂ CO

channel. Thus, from here on, we use this cross section to estimate the rate of dissociation. In Figures 15 and 16 we show some of the results obtain at high CO₂ content, comparing α and E/N for different currents, flows and argon content. We can see that the model is able to qualitatively describe the variations of conversion and reduced electric field for different working conditions. We also use the data obtained with TDLAS at low CO₂ content to validate the model (see Figure

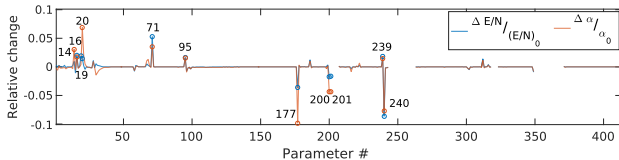


Figure 14: Relative variation of E/N , α , and n_{Ar^m} at 2 Torr, 10 mA, 4 sccm and 25% CO₂ increasing each input parameters 10%.

17). The densities are in all cases underestimated by the model but, again, a qualitative agreement is achieved.

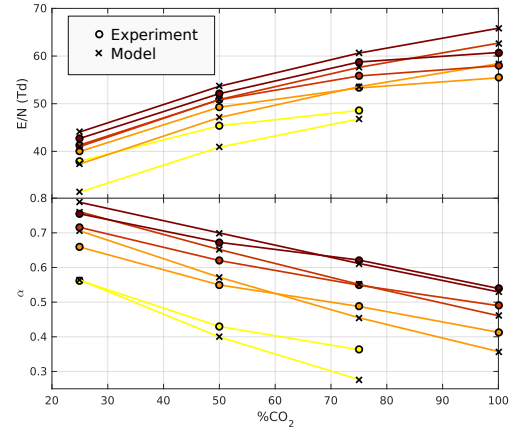


Figure 15: At 5 Torr and 4 sccm.

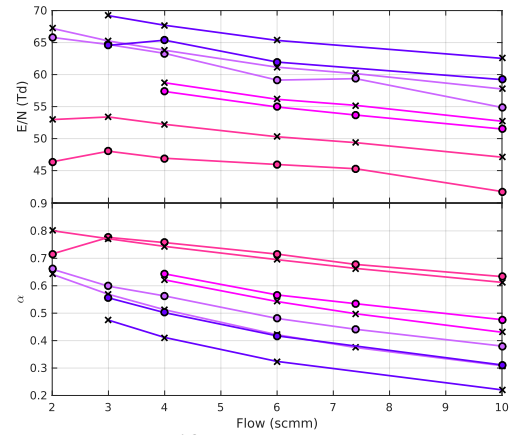


Figure 16: At 2 Torr and 30 mA

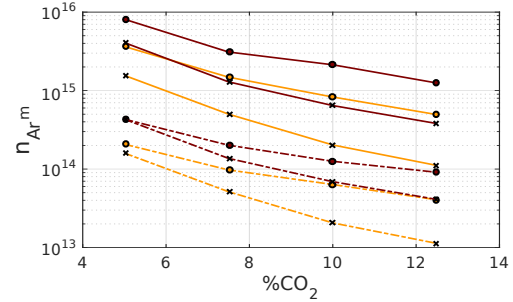


Figure 17: Densities for different currents and Argon content.

Sensitivity analysis

One reaction can have multiple parameters, e.g. a rate coefficient of the form $a \times e^{-b/T_g}$ is considered here to have two parameters: a and b . In this section we try to quantify how sensitive the model is to variations of these parameters. As the number of inputs is too large, we run the model once for a given working condition and then run again increasing each input parameter at a time by 10%. In Figure 14 we show the relative change of the outputs after changing a given input parameter.

We decided to keep for the sensitivity analysis the 10 variables that most affected: conversion, reduced electric field and density of the Argon metastables. The list of reactions associated with those parameters is presented on Table 3.

Parameter #	Reaction description
14	$e + \text{CO}_2 \rightarrow e + \text{CO}_2(\epsilon 1)$
16	$e + \text{CO}_2 \rightarrow e + e + \text{CO}_2^+$
19	$e + \text{CO} \rightarrow e + \text{CO}$
20	$e + \text{CO} \rightarrow e + \text{CO}(a)$
28	$e + \text{CO} \rightarrow e + e + \text{CO}^+$
71	$e + \text{O}_2 \rightarrow e + e + \text{O}_2^+$
95	$e + \text{Ar} \rightarrow e + \text{Ar}$
96	$e + \text{Ar} \leftrightarrow e + \text{Ar}(^3P_2)$
98	$e + \text{Ar} \leftrightarrow e + \text{Ar}(^3P_0)$
177	$e + \text{CO}_2 \rightarrow e + \text{CO} + \text{O}$
186	$e + \text{O}_2(a) \rightarrow e + \text{O}_2^+$
200,201	$\text{CO} + \frac{1}{2}\text{O}_2 \rightarrow \text{CO}_2$
239,240	$e + \text{CO}_4^+ \rightarrow \text{CO}_2 + \text{O}_2$
312	$\text{O}_2^+ + \text{Wall} \rightarrow \text{O}_2$

Table 3: Table with the processes that most affect E/N , α , $n_{Ar(^3P_2)}$ and $n_{Ar(^3P_0)}$

The list is comprised of the leading mechanisms of creation and destruction of CO and Ar^m : electron impact excitation in the case of Ar^m and, in the case of CO, dissociation via direct electron impact and renewal of CO_2 . Reactions with ions and excitation cross section with significant amplitude as well as elastic processes of the dominant species, are also on the list. This is because the cross sections change the EEDF, which then leads to variations of the reduced electric field and in the rate coefficients of electron impact processes. We can see that, while most of the variables are not changing the output significantly, some of them are causing changes as big as the variation of the input variable (10%) or, in the cases of the metastables density, the changes go up to 70%. This already sheds some light into the sensibility of these outputs and justifies this study.

We do 5 random Morris walks for 13 different experimental conditions and compute the corresponding 5 elementary effects. These walks are restricted to changes of less than 5% relative to the unchanged reaction scheme. In Figure 18 we show the results for the mean and standard deviation for one specific working condition.

From the figure, looking at the mean elementary effects, we take similar conclusions in Figure 14. Looking at the standard deviations we also see that some of the inputs are not only changing the outputs but are also doing so differently depending on the other input parameters. This is the case of the cross sections for dissociation and for excitation of $\text{CO}(a)$.

Error estimation

Considering that all the rate coefficients and cross section listed in Table 3 can be assumed to have at least 5% error, we can use the random walks of the last section to estimate an error for the output variables. We do so by computing the difference between the maximum and the minimum outputs obtained for the different sets of input parameters, i.e. $E_{mod}(x) = \frac{\max(y(x)) - \min(y(x))}{y(x_0)}$. In Table 4 we show the mean error for the 13 different working conditions. We also computed the mean er-

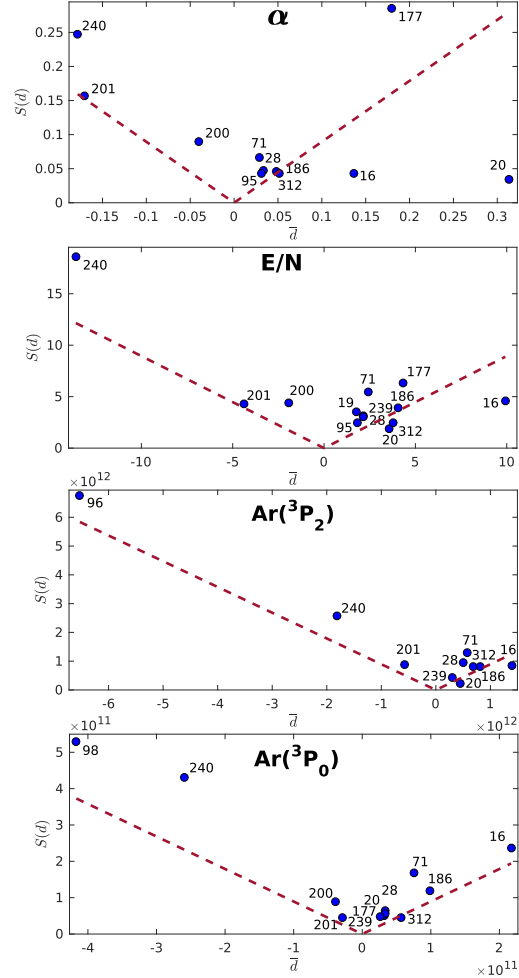


Figure 18: Elementary effects for 2 Torr, 10 mA, 25% CO_2 and 4 sccm.

ror relative to the experimental data, as before, for the different points in the 5 random walks.

	μE_{mod}	σE_{mod}
α	21.8%	15.9%
E/N	12.3%	4.9%
$\text{Ar}(^3P_2)$	132.0%	28.1%
$\text{Ar}(^3P_0)$	200.58%	32.3%

Table 4: Mean and standard deviation of E_{mod} obtained for 13 different working conditions.

From the table we conclude that variations smaller than 5% in the input parameters induced a 20% error in the value of conversion. Also, errors as high as 100% were obtained in the case of the densities of the metastable of Argon.

Why does Ar improve dissociation?

Considering the model validated by the experimental data we now analyse the outputs of the model. We see that the most important dissociation channels, regardless of working condition, accounting for 99% of the dissociation, are:

- $e + \text{CO}_2 \rightarrow e + \text{CO} + \text{O} \approx 75\%$;
- $\text{CO}(a) + \text{CO}_2 \rightarrow 2\text{CO} + \text{O} \approx 25\%$,

which means that Argon metastable states are not improving dissociation via collisions with CO_2 . Also, the

addition of argon strongly modifies the EEDF, as we can see on Figure 19.

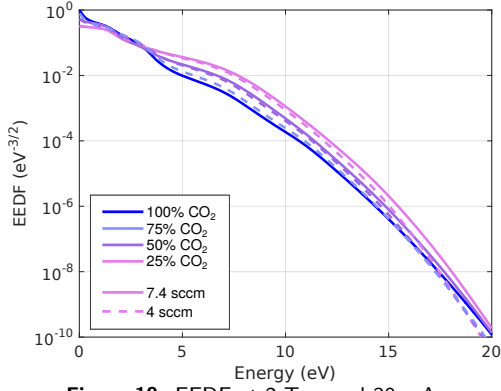


Figure 19: EEDF at 2 Torr and 30 mA.

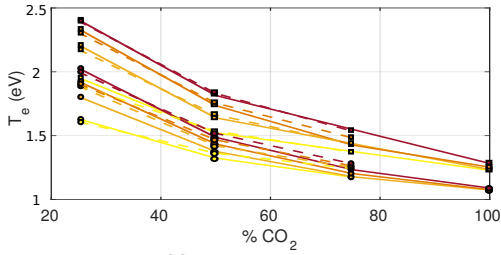


Figure 20: Electron temperature.

As more Argon is added to the plasma, the higher the tail of the distribution function. Therefore, the addition of Argon increases the electron temperature from about 1 eV to 2 eV (Figure 20). Also, we not only have electrons with more energy, but also more electrons overall, although this last effect is less significant. Adding Argon will enhance dissociation by increasing the rates of electron impact dissociation and the rate of electronic excitation of CO, increasing the two most important mechanisms of dissociation. We plot these rates as given by the model for several different working conditions on Figure 21.

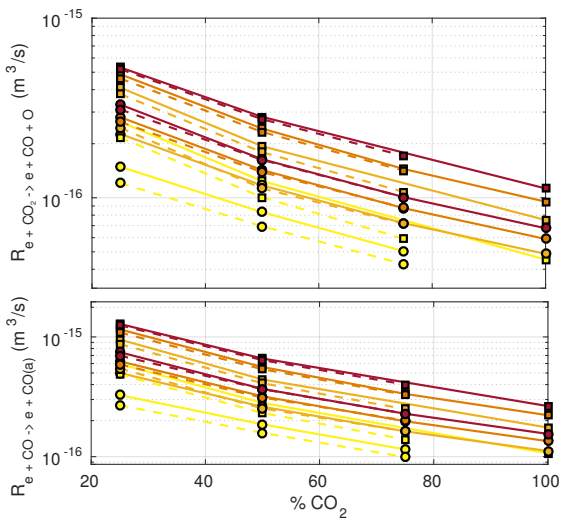


Figure 21: Rates of electron impact reactions.

The change in the EEDF can also explain the slight increase in T_3 experimentally observed due to increase of e-V excitation. Regarding energy consumption within the plasma, we plot on Figure ?? the power spent by electronson different channels.

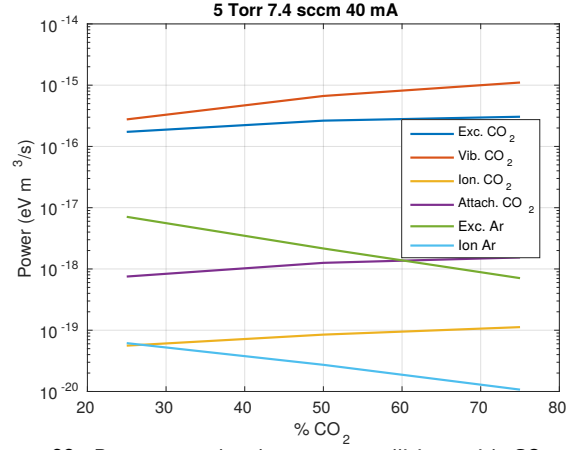


Figure 22: Power spent by electrons on collisions with CO₂ and Ar.

This plot corroborates the previous prediction that Argon does not consume a large portion of the energy of the discharge. Moreover, if the goal is to selectively excite vibrational modes in a low-pressure glow discharge, adding argon is not the way to go. Looking again at the EEDF in Figure 19 we see that Argon increases the tail of the distribution function at the cost of a diminishing bulk, with the fraction of electrons with the typical energies for vibrational excitation - ≈ 1 eV (see Figure 2) - decreasing significantly with Argon addition. In the last figure this appears as a decrease in the power spent on vibrational excitation as more Argon is added to the plasma.

Conclusions

This work focus on the study of the CO₂/Ar mixture in DC glow discharges at low pressure. We aimed to study the dissociation of CO₂ at different pressures (2 to 5 Torr), currents (10 to 40 mA), Argon content (25 to 100% Ar) and flows (2 to 10 sccm), using the characterization of the plasma via experiments and diagnostics on one hand, and modelling tools on the other.

The experiments returned reproducible measurements that we believe to be accurate and that enable us to characterize the plasma at high and low Argon content. The experimental results show that dissociation of CO₂ is greatly improved by Argon addition across the different working conditions. However, adding Argon hampers energy efficiency of the CO₂ dissociation process. Moreover, gas temperatures, as well as the vibrational temperatures of the symmetric stretch and bending modes of CO₂, drop about 50 K from 0 to 75% Argon added, while the temperature of the asymmetric stretch mode increases. Also, the reduced electric field measured decreases about 20 Td.

The model used was able to qualitatively reproduce the variations of α , E/N and n_{Ar^m} due to variations of pressure, current, flow and Argon content. We obtain a small mean error of conversion and reduced electric field between model and experiment of the order of 10%. The sensitivity analysis results show that variations on the input parameters of the model as small as 5% induce significant errors on α , E/N , $n_{Ar(^3P_2)}$ and $n_{Ar(^3P_2)}$ that are of the order of or smaller than the errors between

model and experiment. This shows, on the one hand, the necessity of the use of accurate cross sections and rate coefficients and, on the other, that the differences between model and experiment obtained are reasonable given the sensibility of the model.

Moreover, we use the model to derive some conclusions on how exactly is Argon improving CO₂ conversion. The model results show that the most important mechanisms of dissociation on this type of set up are electron impact dissociation ($\approx 75\%$ contribution) and dissociation through collision of CO₂ with CO(a) ($\approx 25\%$). The addition of Argon modifies significantly the electron energy distribution function: with more Argon more electrons are created and each electron is on average more energetic. Thus, Argon influences dissociation of CO₂ by enhancing the rates of electron impact dissociation and electron impact of excitation of CO.

Regarding dissociation via vibrational excitation, the addition of Argon does not seem to change vibrational excitation on a significant manner. Although there is a measurable increase in the temperature of the asymmetric stretch mode that seems to be explainable with an increase of electron impact excitation of CO₂, the increase is of only about some tens of K. That coupled with the fact that we did not need to include the vibrational states to explain the increase of dissociation due to argon addition, points to the conclusion that the vibrational ladder climbing process is not causing significant dissociation in this particular set-up.

Acknowledgements

This work has been done within the LABEX PLAS@PAR project, and received the financial state aid managed by the ANR, as part of the programme "Investissements d'avenir" ANR-11-IDEX-0004-02. This work was also partially supported by the Portuguese FCT, under Projects UID/FIS/50010/2013, PTDC/FIS-PLA/1420/2014 (PREMIERE) and PTDC/FISPLA/1243/2014 (KIT-PLASMEBA).

References

- [1] Thomas Stocker. Cambridge University Press, 2014.
- [2] Ramses Snoeckx et al. In: *Chem. Soc. Rev.* 46 (19 2017), pp. 5805–5863.
- [3] Waldo Bongers et al. In: *Plasma processes and polymers* 14.6 (2017), p. 1600126.
- [4] Robby Aerts et al. In: *The Journal of Physical Chemistry C* 116.44 (2012), pp. 23257–23273.
- [5] Tomáš Kozák et al. In: *Plasma Sources Science and Technology* 24.1 (2015), p. 015024.
- [6] Peter Koelman et al. In: *Plasma Processes and Polymers* 14.4-5 (2017), p. 1600155.
- [7] PA Sá et al. In: *Journal of Physics D: Applied Physics* 37.2 (2003), p. 221.
- [8] B L M Klarenaar et al. In: *Plasma Sources Science and Technology* 26.11 (2017), p. 115008.
- [9] Matthew Moss et al. In: *Plasma Sources Science and Technology* (Jan. 2017).
- [10] Huali Long et al. In: *international journal of hydrogen energy* 33.20 (2008), pp. 5510–5515.
- [11] Leonard B Loeb. John Wiley & Sons, 1939.
- [12] A. Fridman. Cambridge University Press, 2008.
- [13] IST cross-section database. Available at <https://fr. www.lxcat.net/>. Accessed: 2018-03-03.
- [14] DCM van den Bekerom. In: (2018). PhD thesis.
- [15] Marleen Ramakers et al. In: *Plasma Processes and Polymers* 12.8 (2015), pp. 755–763.
- [16] N. R. Pinhão et al. In: *Plasma Chemistry and Plasma Processing* 31.3 (2011), pp. 427–439.
- [17] H Martinez et al. In: *Physics of Plasmas* 24.4 (2017), p. 043508.
- [18] Thomas G Beuthe et al. In: *Japanese Journal of applied physics* 36.7S (1997), p. 4997.
- [19] Michael A. Lindon et al. In: *Frontiers in Physics* 2 (2014), p. 55.
- [20] Yuxuan Zeng et al. In: *Journal of Physics D: Applied Physics* 50.18 (2017), p. 184004.
- [21] Shaojun Xu et al. In: *Chemical Engineering Journal* 327.Supplement C (2017), pp. 764 –773.
- [22] O Taylan et al. In: *Plasma Sources Science and Technology* 24.1 (2015), p. 015006.
- [23] Nader Sadeghi. In: *J. Plasma Fusion Res.* 80.9 (2004), pp. 767–776.
- [24] P Coche et al. In: *Journal of Physics D: Applied Physics* 49.23 (2016), p. 235207.
- [25] Max D Morris. In: *Technometrics* 33.2 (1991), pp. 161–174.
- [26] T. O'Haver. <https://terpconnect.umd.edu/~toh/spectrum/functions.html>. Accessed: 2018-06-01.
- [27] Adriana Annušová et al. In: *Plasma Sources Science and Technology* 27.4 (2018), p. 045006.
- [28] Polina Ogloblina et al. In: XXXIII ICPIG 2017 (2017).
- [29] Ángel Yanguas-Gil et al. In: *Journal of Physics D: Applied Physics* 38.10 (2005), p. 1588.
- [30] Marco Antonio Ridenti et al. In: *Physical Review E* 97.1 (2018), p. 013201.
- [31] J Gregório et al. In: *Plasma Sources Science and Technology* 21.1 (2012), p. 015013.
- [32] WL Wiese et al. In: *Physical Review A* 39.5 (1989), p. 2461.
- [33] CM Ferreira et al. In: *Journal of applied physics* 57.1 (1985), pp. 82–90.
- [34] Kinga Kutasi et al. In: *Journal of Physics D: Applied Physics* 43.17 (2010), p. 175201.
- [35] Marija Grofulović et al. In: *Journal of Physics D: Applied Physics* 49.39 (2016), p. 395207.
- [36] Yukikazu Itikawa. In: *Journal of Physical and Chemical Reference Data* 31.3 (2002), pp. 749–767.
- [37] A Cenian et al. In: *Contributions to Plasma Physics* 35.3 (1995), pp. 273–296.
- [38] JH Schummers et al. In: *Physical Review A* 7.2 (1973), p. 683.
- [39] C Lee et al. In: *Journal of Vacuum Science & Technology A: Vacuum, Surfaces, and Films* 13.2 (1995), pp. 368–380.
- [40] LS Polak et al. In: *International Journal for Radiation Physics and Chemistry* 8.1-2 (1976), pp. 257–282.